

1
2 **Supplementary information:**
3 **Tracking Brownian motion in three dimensions and characterization of individual**
4 **nanoparticles using a fiber-based high-finesse microcavity**

5 Larissa Kohler,¹ Matthias Mader,^{2,3} Christian Kern,^{4,5} Martin Wegener,^{4,5} and David Hunger^{1,6,*}

6 ¹*Karlsruher Institut für Technologie, Physikalisches Institut,*
7 *Wolfgang-Gaede-Str. 1, 76131 Karlsruhe, Germany*

8 ²*Fakultät für Physik, Ludwig-Maximilians-Universität, Schellingstraße 4, 80799 München, Germany*

9 ³*Max-Planck-Institut für Quantenoptik, Hans-Kopfermann-Str. 1, 85748 Garching, Germany*

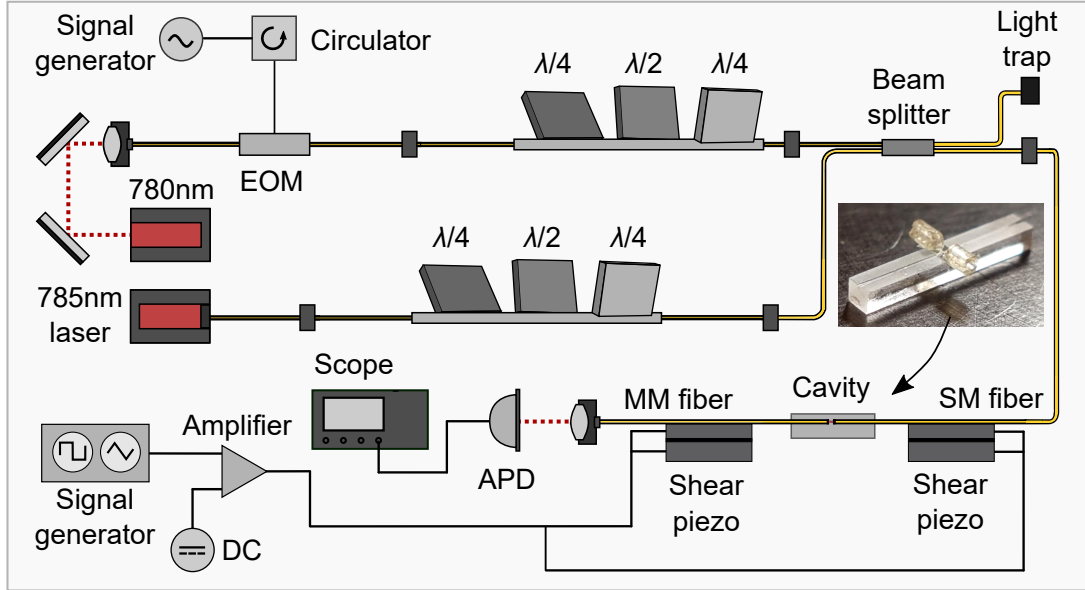
10 ⁴*Karlsruher Institut für Technologie, Institut für Angewandte Physik,*
11 *Wolfgang-Gaede-Str. 1, 76131 Karlsruhe, Germany*

12 ⁵*Karlsruher Institut für Technologie, Institut für Nanotechnologie,*
13 *Hermann-von-Helmholtz-Platz 1, 76344 Eggenstein-Leopoldshafen, Germany*

14 ⁶*Karlsruher Institut für Technologie, Institut für QuantenMaterialien und Technologien ,*
*Hermann-von-Helmholtz-Platz 1, 76344 Eggenstein-Leopoldshafen, Germany**

* david.hunger@kit.edu

15 **Supplementary Figure 1: Laser and detection system**

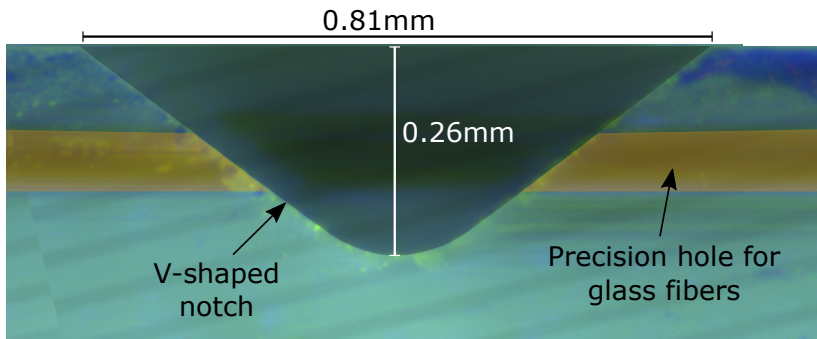


16 Schematic representation of the measurement setup. The cavity can be probed
 17 simultaneously by two different lasers: A tunable grating stabilized external cavity
 18 diode laser at $\lambda = 780$ nm (TOPTICA DLpro) and a wavelength stabilized laser
 19 diode (Thorlabs LP785-SAV50) at $\lambda = 785$ nm. The 780 nm laser beam is coupled
 20 into a singlemode fiber and its polarization can be changed with a fiber polarization
 21 controller ($\lambda/4 - \lambda/2 - \lambda/4$). A 90/10-beamsplitter (Thorlabs TN785R2A2) allows
 22 the coupling of both wavelengths into the cavity singlemode (SM) fiber. Without
 23 the need of any coupling optics, the light is directly coupled into the cavity. The
 24 transmitted light from the cavity is then collected by a multimode (MM) fiber, de-
 25 tected with an avalanche photodiode (Thorlabs APD 110A/M) and recorded by
 26 an oscilloscope (LeCroy HRO66Zi).

27 Each cavity fiber is clamped on a piezo-electric actuator. The actuators are operated
 28 in opposite directions to change the cavity length. Here we are using a triangular
 29 voltage signal for the operation of the actuators, which is generated by a signal
 30 generator and amplified (Falco Systems WMA-280).

31 The laser can be phase-modulated by an electro-optic modulator (EOM, Laser Com-
 32 ponents NIR-MPX800) to produce sidebands at precisely known frequency separa-
 33 tions, which allow us to calibrate the resonance linewidth in frequency units.

34 **Supplementary Figure 2: Fabrication of the first cavity system by direct**
 35 **laser writing**



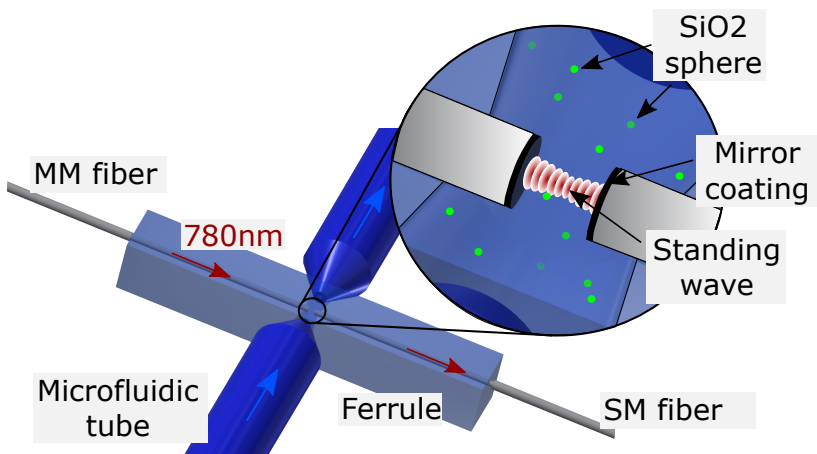
36 In the following, we describe the fabrication of the cavity system shown in Fig. 1a
 37 and b (cavity 1), which comprises a glass ferrule allowing for the precise alignment
 38 of the optical fibers forming the cavity and a microfluidic channel, which is oriented
 39 perpendicular to the cavity.

40 In the first step, using an automatic dicing saw (Disco DAD3350), we cut a v-shaped
 41 notch into the central part of the glass ferrule, which gives access to the cavity. A
 42 corresponding micrograph is shown in the figure above.

43 In the second step, we fabricate the microfluidic channel using a commercial di-
 44 rect laser writing setup (Photonic Professional GT, Nanoscribe GmbH) with a
 45 $25\times$ NA 0.8 objective lens (LCI Plan-Neofluar Imm Corr DIC M27, Carl Zeiss Mi-
 46 croscopy GmbH) and the liquid negative-tone photoresist IP-S (Nanoscribe GmbH).
 47 The total writing time is about 3.5 h. Due to the large dimensions of the polymer
 48 structure, several measures have to be taken: First, we use a galvanometer mirror
 49 scanning system to increase the writing speed. Second, we use the so-called dip-in
 50 configuration, which means that the objective lens is immersed in the liquid photo-
 51 resist itself, thereby removing the constraint on the height of the structure imposed
 52 by the working distance of the objective lens. Third, instead of polymerizing the
 53 whole structure during the actual writing process, we only polymerize an outer shell
 54 as well as an internal support scaffold. Following the development of the structure
 55 in mrDev 600 (micro resist technology GmbH), the liquid photoresist inside of the
 56 structure is cured using a UV flood-exposure.

57 In the third and last step, in order to ensure that the system is watertight, we apply
 58 a hydrophobic coating in a two-step process: First, the structure is conformally
 59 coated with a Al_2O_3 layer with a thickness of several ten nanometers using atomic-
 60 layer deposition. Second, following a brief air-plasma treatment, the structure is
 61 immersed in a 3 mM solution of octadecyltrichlorsilane (CAS 112-04-9) in toluene.

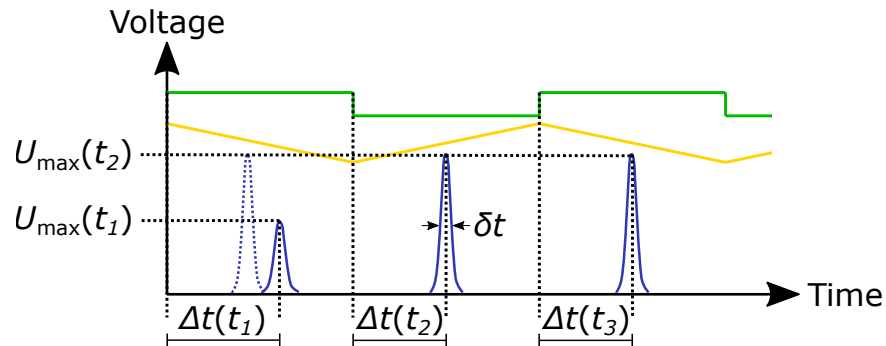
62 **Supplementary Figure 3: Cavity system with a drilled hole for the**
 63 **microfluidic channel**



64 Our experimental data was recorded by two different cavity setups (see Supple-
 65 mentary Note 1). Both setups incorporate a glass ferrule with a precision hole, into
 66 which we insert the cavity fibers opposite of each other. In contrast to the photore-
 67 sist structure of the setup shown in Fig. 1a, here, the microfluidic section consists
 68 of a cone-shaped hole, which is drilled into the glass ferrule by a femtosecond laser.
 69 The microfluidic hole has a mean outer diameter of 560 μm , a mean inner diameter
 70 of 320 μm and intersects the existing precision hole orthogonally in the center of
 71 the ferrule. Commercially available microfluidic tubes are directly attached to the
 72 microfluidic access from each side.

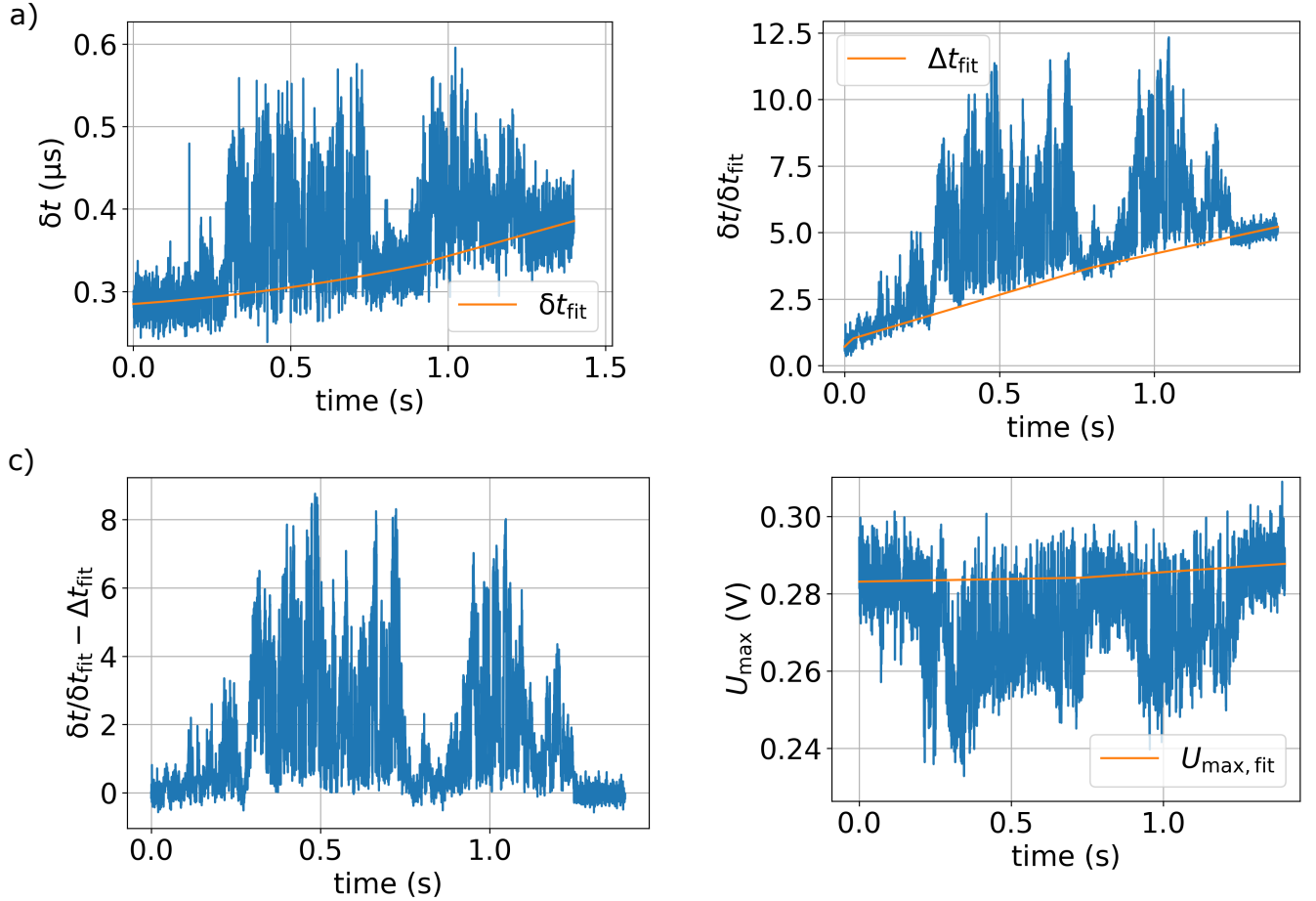
73

74 **Supplementary Figure 4: Extracting time shift and decrease of ampli-**
 75 **tude from the detection signal**



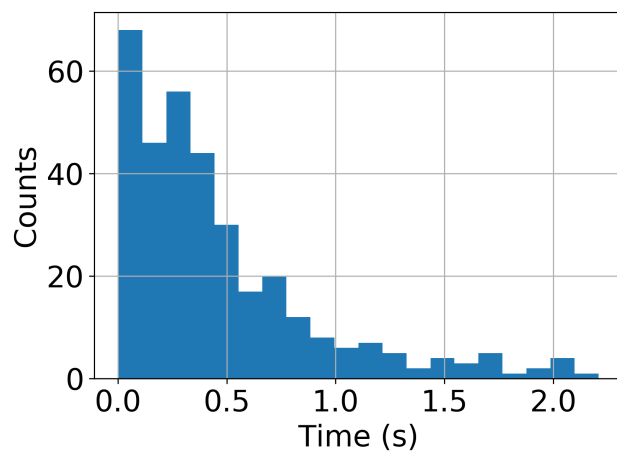
76 For the measurement of the cavity frequency shift and transmission change, the
 77 cavity length is modulated with a triangular voltage driving two shear piezo-electric
 78 actuators with a frequency of 3 kHz (yellow). Only when the cavity length hits the
 79 resonance condition, the fundamental mode (blue) occurs and can be detected on
 80 the photodiode. On each trigger event (green), one sweep action of the piezos is
 81 executed. If the cavity is empty (no particle inside the light field), the resonance
 82 peak height remains unchanged ($U = \text{const.}$), but changes its temporal position
 83 Δt due to thermal, acoustic, mechanical and electronic noises mostly at low fre-
 84 quencies. These drifts are then removed by a background subtraction method (see
 85 Supplementary Fig. 5). In the schematics, the drift is considered to be constant.
 86 The empty cavity condition is shown in the figure at the trigger times t_2 and t_3 .
 87 If a nanoparticle enters the cavity light field, it produces a decrease of the reso-
 88 nance amplitude and a temporal shift (see trigger event at t_1), which corresponds
 89 to a change of the resonance condition of the cavity length. In our experiments,
 90 we measure the amplitude value U_{\max} , the temporal position Δt and the resonance
 91 linewidth δt for each trigger event at time steps of 0.33 ms. Using the sidebands
 92 produced by the phase modulation, we convert the measured temporal shift Δt into
 93 a frequency shift $\Delta \nu$ (see Supplementary Fig. 5).

94 **Supplementary Figure 5: Data evaluation for nanoparticle transit**
 95 **events**



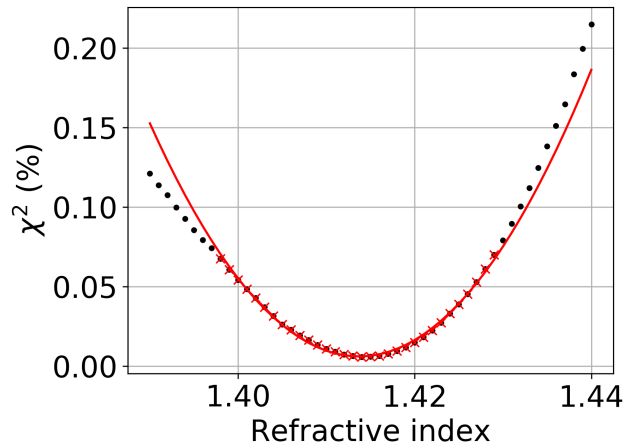
96 Each nanoparticle transit event produces a change in the resonance linewidth δt ,
 97 resonance amplitude U_{\max} and cavity length depending on the nanoparticle position
 98 inside the light field. The cavity length change is measured as a temporal shift
 99 Δt (see Supplementary Fig. 4). Supplementary Fig. 5a shows δt over time and a
 100 parabola fit to the undisturbed section of the measurement of the linewidth (empty
 101 cavity), b) shows the temporal shift in units of cavity temporal linewidths $\delta t/\delta t_{\text{fit}}$
 102 over time and a parabola fit to the undisturbed section of the measurement of the
 103 temporal linewidths and c) shows the drift corrected shifts $\delta t/\delta t_{\text{fit}} - \Delta t_{\text{fit}}$. This is
 104 converted into a frequency shift by the calibration described above (Supplementary
 105 Fig. 1, 4). d) shows U_{\max} over time and a parabola fit to the amplitude values of
 106 the undisturbed cavity. The transmission change is defined as

$$\Delta T(t)/T_0 = 100\% \times \left(1 - \frac{U_{\max}(t)}{U_{\max,\text{fit}}(t)} \right).$$

107 **Supplementary Figure 6: Time duration of the measured transit events**

108 A measured transit event is shown in Supplementary Fig. 5c. From each transit
109 event, the dwell time of the nanoparticle inside the cavity is determined (signal >
110 noise) and all 330 transit events are plotted in the histogram above.

111 **Supplementary Figure 7: Determination of the refractive index from**
 112 **the measured decrease of amplitudes**



114 For the measurement of the SiO₂ nanoparticles with $r_{\text{hydr}} = 71.5$ nm (sample A)
 115 we used the cavity shown in Fig. 1 with a finesse of $\mathcal{F} = 18400$ and a cavity length
 116 of 27.3 μm . Due to the fabrication, our cavity mirrors are not perfectly spherical at
 117 the center and exhibit different radii of curvatures (ROC) r_c :

	$r_{c,x}$ (μm)	$r_{c,y}$ (μm)
SM-Fiber	62.4	56.6
MM-Fiber	58.9	131.0

119 The calculated impact on the transmission change values for the given ROCs
 120 are negligible small. Hence, we can use the mean values $\langle r_{c,\text{SM}} \rangle = 59.5$ μm and
 121 $\langle r_{c,\text{MM}} \rangle = 95.0$ μm for the determination of the refractive index n_p from the exper-
 122 imental data in Fig. 2c. In the figure above, the $\chi^2(n_k)$ -function is shown. Here
 123 we compare different simulations with fixed particle radius and different refractive
 124 indices $\Delta T(\nu_i, n_k)$ (see Supplementary Note 2) with the mean transmission change
 125 $\langle \Delta T(\nu_i) \rangle$ at each frequency shift (see black dashed line in Fig. 2c:

$$\chi^2(n_k) = \sum_i \frac{|\Delta T(\nu_i, n_k) - \langle \Delta T(\nu_i) \rangle|^2}{\langle \Delta T(\nu_i) \rangle}$$

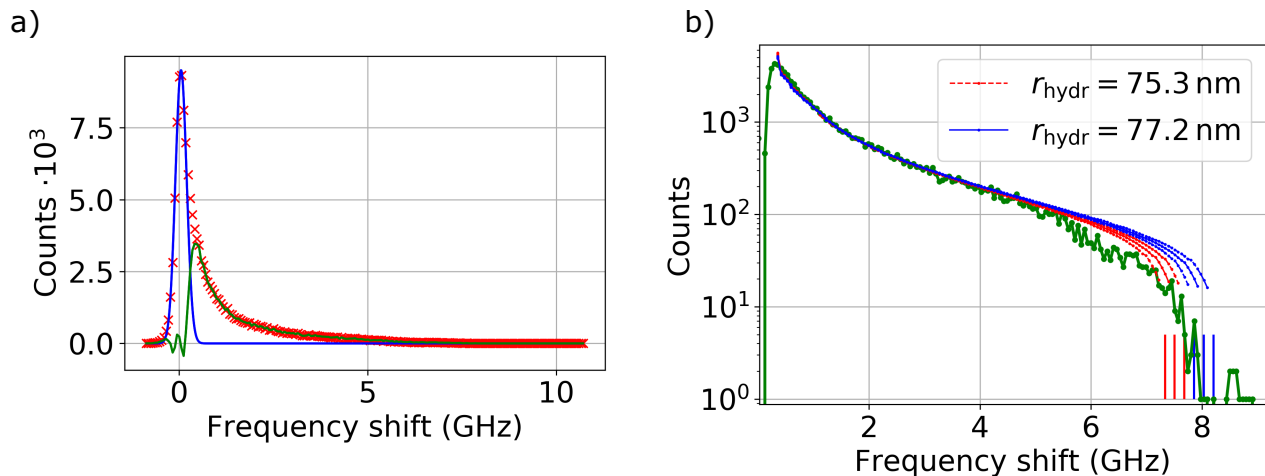
126 A parabola fit (red) to the center of the minimum (red crosses) gives the value
 127 $n_p = 1.41 \pm 0.01$. The error is deduced from the y -error of the parabola fit.

Supplementary Figure 8: Determination of the refractive index from the measured frequency shifts

With the cavity shown in Supplementary Fig. 3 with a finesse of $\mathcal{F} = 56710$ and a cavity length of $5.4 \mu\text{m}$, we measured the frequency shift of the fundamental mode produced by SiO_2 nanoparticles with $r_{\text{hydr}} = 75.3 \text{ nm}$ (sample B). Since we simultaneously measure the position of two higher order cavity modes in addition here, our data acquisition was not able to measure also the transmission change correlated to the frequency shifts, such that we have to extract the refractive index only from the measured frequency shifts. Here we have to consider the frequency shifts for different ROCs:

	$r_{c,x}$ (μm)	$r_{c,y}$ (μm)
SM-Fiber	46.1	53.1
MM-Fiber	79.2	87.8

This leads to a larger error for the refractive index and can be avoided in future experiments by always measuring the decrease of amplitude (see Supplementary Fig. 7).



In a) we show a histogram of the measured frequency shifts (red crosses) from 59 transit events. The high peak at small frequency shifts arises due to the empty cavity frequency noise of the measurement, and can be fitted by a Gaussian function (blue) and subsequently subtracted from the measured distribution (green). This yields the frequency shifts predominantly produced by the single nanoparticle transits. b) shows the nanoparticle's frequency shifts on a logarithmic scale (green). Here, a characteristic steep decay at 8.05 GHz appears, which corresponds to the maximum measurable frequency shift for a single nanoparticle located at an

151 antinode of the standing wave cavity light field. In order to determine the refractive
 152 index, probability distributions of the theoretical frequency shifts produced by a sin-
 153 gular nanoparticle with different refractive indices are calculated for the mean mirror
 154 curvatures $\langle r_{c,SM} \rangle = 49.6 \mu\text{m}$ and $\langle r_{c,MM} \rangle = 83.5 \mu\text{m}$ (also see Supplementary Note
 155 3). Here we enter for the hydrodynamic radius the maximal value of $r_{\text{hydr}} = 77.2 \text{ nm}$
 156 of the size distribution (see Supplementary Fig. 10, DLS measurement), since the
 157 maximal measured shift tends to occur for particles with large size. The analysis
 158 yields refractive index of $n_p = 1.465$. Taking into account the frequency noise of
 159 0.15 GHz , we get an estimation for the measurement error of $n_{\text{meas,err}} = 0.001$. In
 160 order to evaluate the systematic error, we calculate the refractive indices which
 161 produce the same frequency shift of 8.05 GHz for the different possible ROC com-
 162 binations. We end up with a systematic error of $n_{\text{sys}} = 0.003$. b) shows simulations
 163 for $n_p = 1.453$, $n_p = 1.456$ and $n_p = 1.459$ for $r_{\text{hydr}} = 77.2 \text{ nm}$ (blue) and the mean
 164 hydrodynamic radius $r_{\text{hydr}} = 75.3 \text{ nm}$ (red). For increasing refractive indices the
 165 maximal theoretical frequency shift increases.

Supplementary Figure 9: SiO₂ spheres with $r_{\text{hydr}} = 71.5 \text{ nm}$

Sample A was purchased from microParticles GmbH. The nanoparticles are specified to have a mean hydrodynamic radius of $r_{\text{hydr}} = 71.5 \text{ nm}$.

a) Sample properties provided by the manufacturer

Properties	Silica-Particles
Density	1.85 g/cm ³
Refractive index	1.42
Particle diameter	100 nm – 25 μm
Monodispersity	CV < 5%
Particle shape	spherical
Surface charge	anionic
Functional groups	silanol
Hydrophilicity/Hydrophobicity	hydrophilic
Crosslinking	crosslinked
Porosity	non-porous
Temperature stability	to 1000 °C
Mechanical strength	robust
Solubility in acids and bases	soluble in HF and bases
Stability in solvents without swelling	water, alcohols, all solvents and oils
Biocompatibility	biocompatible

www.microparticles-shop.de

SiO₂-R-0.15

Infos

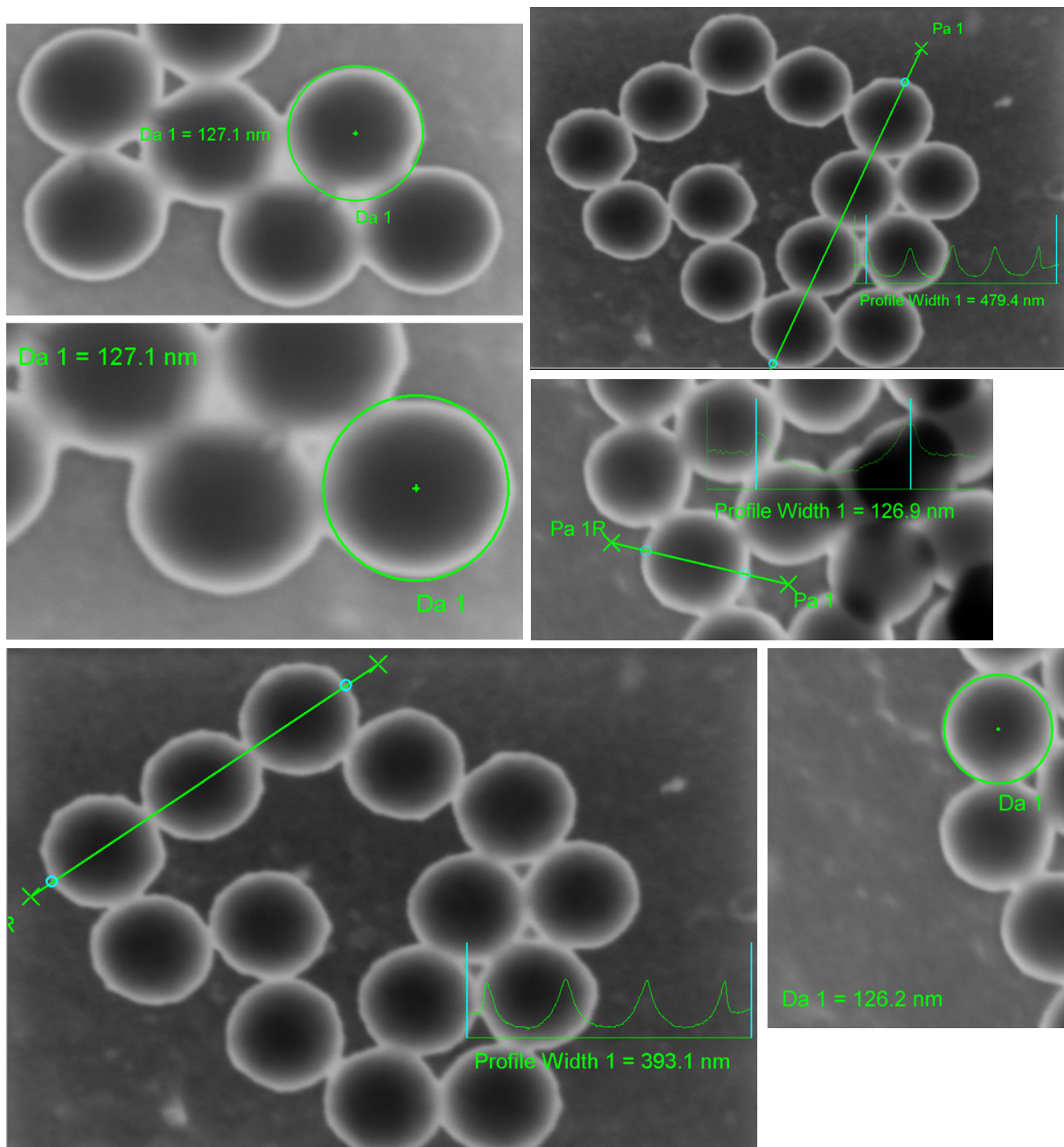
Batch:	SiO ₂ -R-L3205-23
Mean Diameter (μm):	0.143
Standard Deviation (μm):	0.004
CV (%):	3.1
Solids Content (wt.-%):	5

The information shown in the figure was taken from the web page www.microparticles-shop.de (June, 2020). We got additional information via email transfer:

The refractive index of the SiO₂ nanoparticles was determined by refractive index matching and their size distribution was determined by DLS measurements.

176

b) SEM measurements



177

178

179

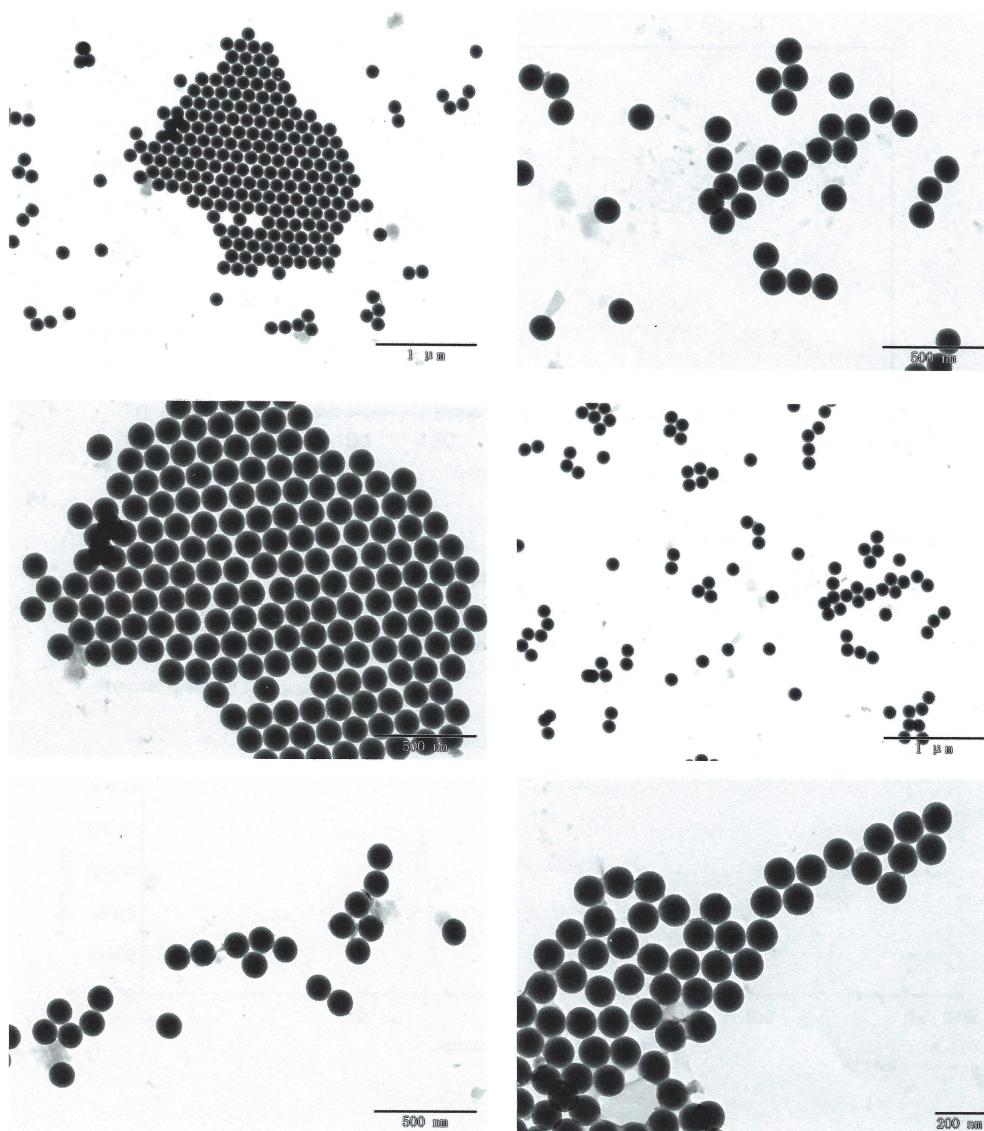
The figure above shows SEM pictures of the SiO₂ nanoparticles, which are dried on a graphene grating. The measured mean radius is $r_{\text{SiO}_2} = 63.5 \text{ nm}$ and thus smaller than the hydrodynamic radius of 71.5 nm provided by the supplier.

Supplementary Figure 10: SiO₂ spheres with $r_{\text{hydr}} = 75.3 \text{ nm}$ 

Aug 20, 2019

Non-Functionalized Colloidal Silica Nanospheres (120 nm)

Transmission electron micrographs:



Page 6 of 11

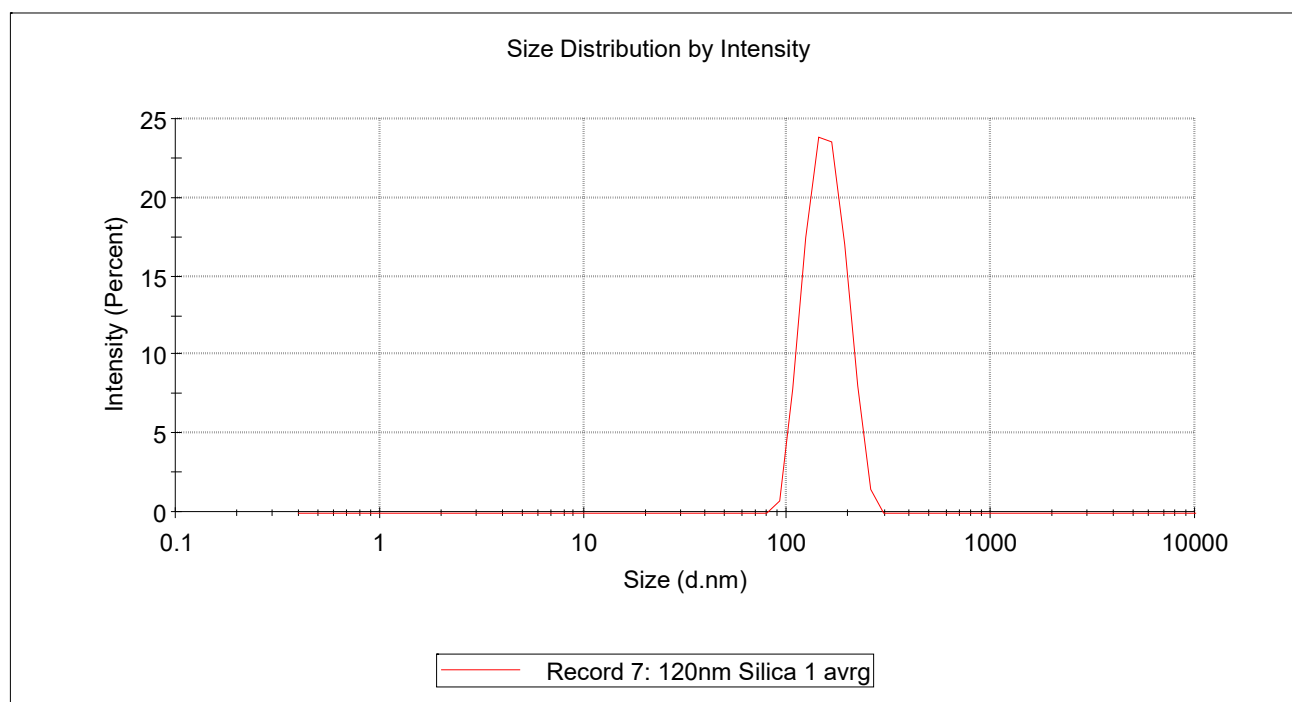
181 Sample B was purchased from ALPHA nanotech. The nanoparticles were charac-
182 terized by TEM by the manufacturer, and a physical radius of $r = 60 \text{ nm}$ is specified.
183 The figure above is taken from the company's data sheet.

184 To independently determine the hydrodynamic radius, we have performed DLS

Results

	Size (d.n...	% Intensity:	St Dev (d.n...
Z-Average (d.nm): 150,6	Peak 1: 156,7	100,0	34,22
PdI: 0,016	Peak 2: 0,000	0,0	0,000
Intercept: 0,963	Peak 3: 0,000	0,0	0,000

Result quality **Good**

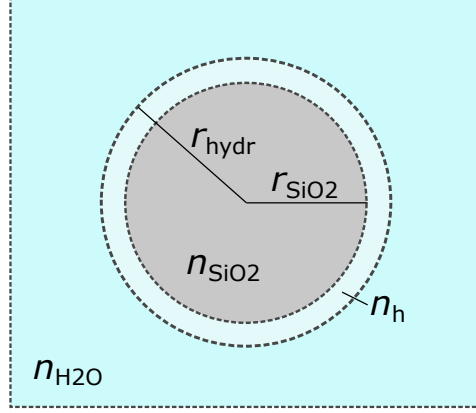


185 measurements of sample B. The z-average yields a hydrodynamic radius of $r_{\text{hydr}} = 75.3 \text{ nm}$
 186 with a standard deviation $\sigma_r = \sqrt{PdI} \cdot r_{\text{hydr}} = 3.8 \text{ nm}$.

187 Via email transfer we got from ALPHA nanotech the information that they didn't
 188 measure the refractive index of the glass nanospheres, but "as there is no impurity
 189 added into the silica nanospheres, the silica nanospheres should have the same phys-
 190 ical parameters as silica materials". Accordingly, we assume the refractive index of
 191 the bulk silica nanospheres to be $n_{\text{SiO}_2} = 1.4537$ (at 780 nm).

192 **Supplementary Figure 11: Hydration shell**

193



194 Due to negative surface charges, a hydration shell is formed when the SiO₂
 195 nanospheres are solved in water. This leads to an increased effective radius
 196 ($r_{\text{hydr}} > r_{\text{SiO}_2}$) as well as to an effective refractive index n_{eff} , which is lower than
 197 the one of the solid sphere. With our cavity sensor, we measure r_{hydr} and n_{eff} . The
 198 value for the intrinsic size r_{SiO_2} can be obtained by scanning electron (sample A,
 199 see Supplementary Fig. 9) or transmission electron micrographs (sample B, see
 200 Supplementary Fig. 10). The value for the refractive indices of the bulk spheres
 201 are $n_{\text{SiO}_2} = 1.42$ (sample A, see Supplementary Fig. 9) and $n_{\text{SiO}_2} = 1.4537$ (sample
 202 B, see Supplementary Fig. 10). Following [1], we can calculate the mean refractive
 203 index n_h of the shell, by solving

$$\frac{n_{\text{eff}}^2 - n_{\text{H}_2\text{O}}^2}{n_{\text{eff}}^2 + 2n_{\text{H}_2\text{O}}^2} = \frac{(2n_h^2 + n_{\text{SiO}_2}^2)(n_h^2 - n_{\text{H}_2\text{O}}^2)r_{\text{hydr}}^3 + (n_{\text{SiO}_2}^2 - n_h^2)(2n_h^2 + n_{\text{H}_2\text{O}}^2)r_{\text{SiO}_2}^3}{(2n_h^2 + n_{\text{SiO}_2}^2)(2n_{\text{H}_2\text{O}}^2 + n_h^2)r_{\text{hydr}}^3 + 2(n_{\text{SiO}_2}^2 - n_h^2)(n_h^2 - n_{\text{H}_2\text{O}}^2)r_{\text{SiO}_2}^3}.$$

We get

$$n_h = \sqrt{-\frac{p}{2} + \sqrt{\frac{p^2}{4} - q}},$$

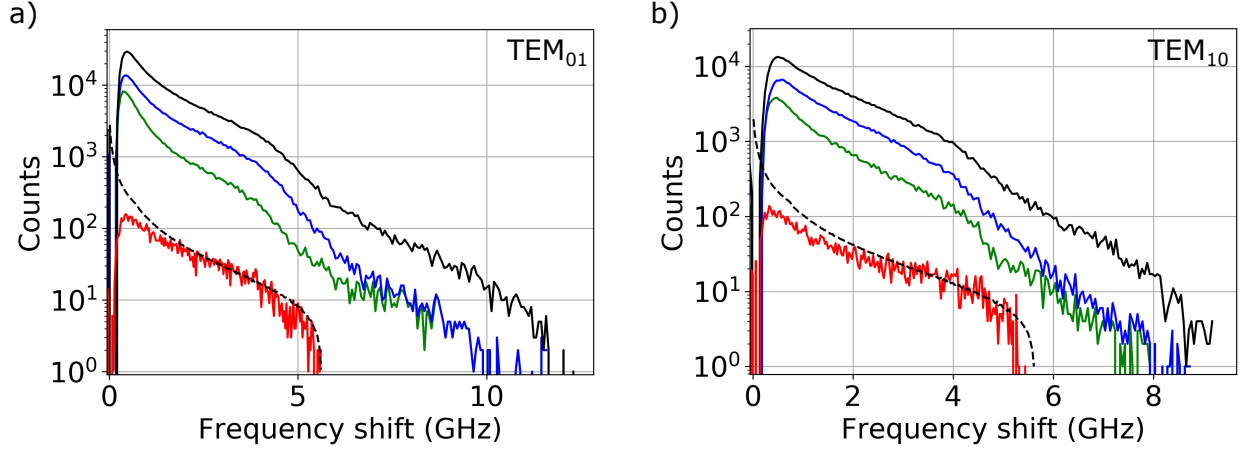
204 with

$$p = \frac{n_{\text{eff}}^2(r_{\text{SiO}_2}^3 + 2r_{\text{hydr}}^3) - n_{\text{SiO}_2}^2(2r_{\text{SiO}_2}^3 + r_{\text{hydr}}^3)}{2(r_{\text{SiO}_2}^3 - r_{\text{hydr}}^3)} \quad \text{and}$$

$$q = -\frac{n_{\text{SiO}_2}^2 n_{\text{eff}}^2}{2}.$$

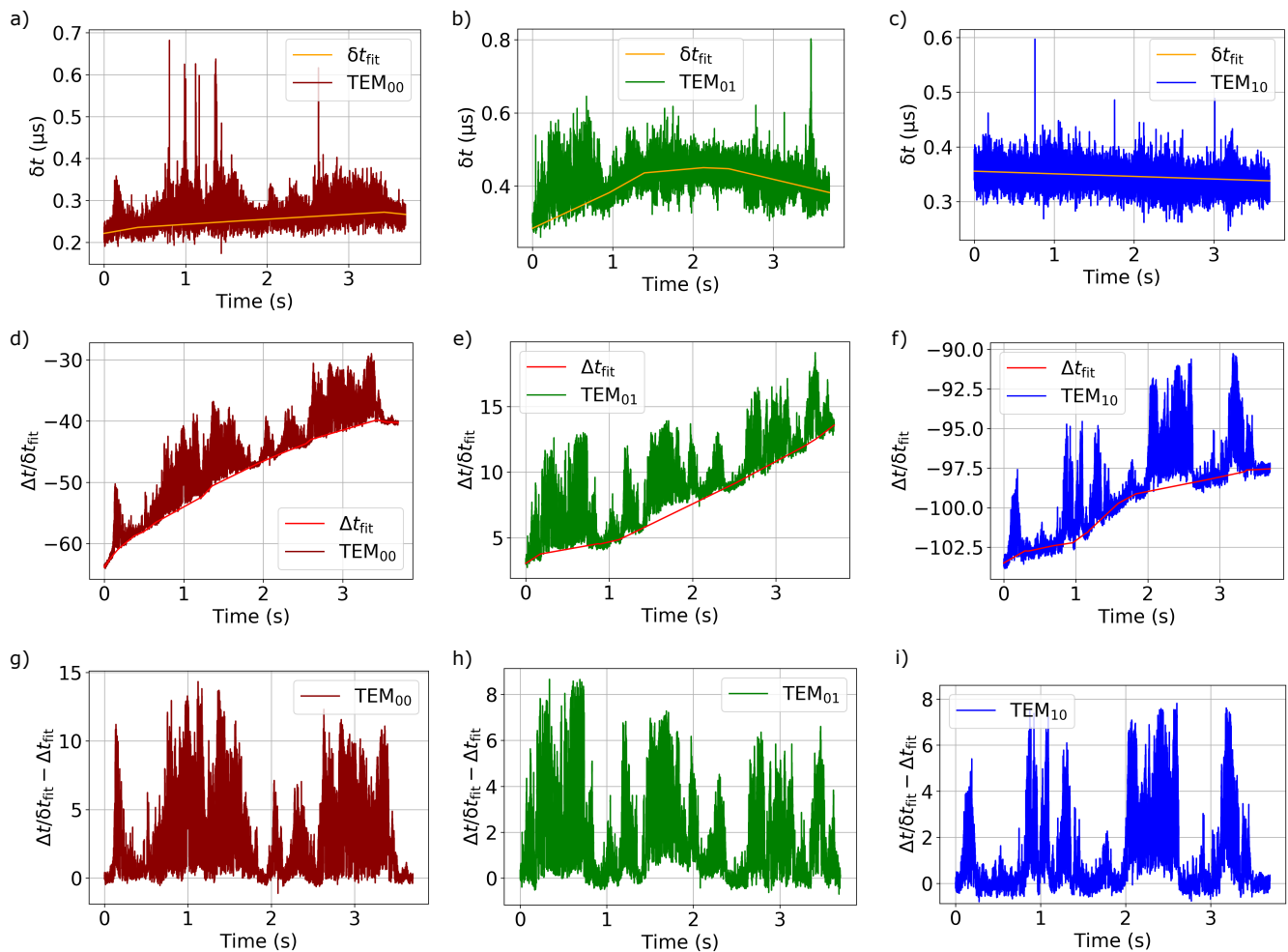
205 We get $n_h = 1.40 \pm 0.04$ for sample A and $n_h = 1.46 \pm 0.01$ for sample B.

Supplementary Figure 12: Temporal evolution of the frequency shift histograms for the higher order transverse modes



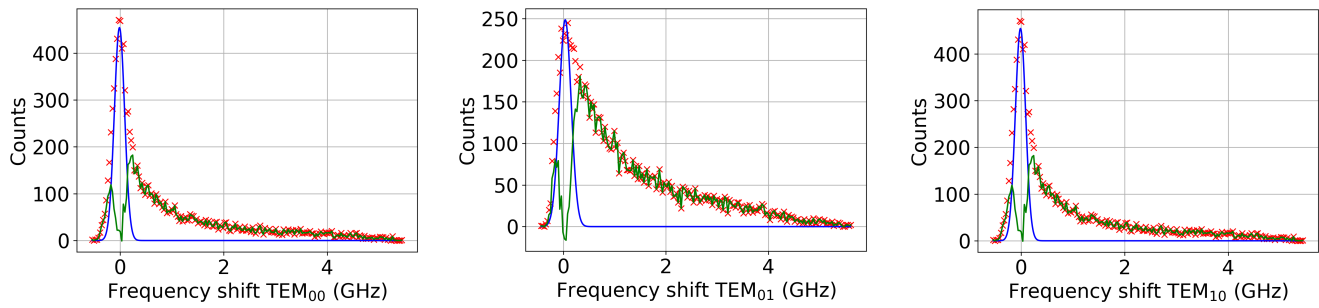
In a) and b) the time evolution of the measured frequency shift probability distributions for the higher order TEM_{01} and TEM_{10} modes are shown. The red solid line shows a single nanoparticle transit event, which is used for the reconstruction of the spatial coordinates of the nanoparticle track (main text Fig. 3b green and blue). It was measured within the first 2 hours. Dashed black line: simulated density of states for a single nanoparticle with refractive index $n_p = 1.46$ and $r_{hydr} = 75.3$ nm, green: frequency shifts of about 59 transits (after 2 hours measurement time), blue: frequency shifts of about 71 additional transits (3 hours) and 4) about 210 additional transits (8 hours). In contrast to the time evolution of the TEM_{00} frequency shifts (see Fig. 2e, blue), the typical steep decay of the density of states for single nanoparticle transits doesn't occur for the first 2 hours measurement time for the higher order modes (Supplementary Fig. 11 a,b green). Since the TEM_{00} mode detects single nanoparticles with a low error probability, we can exclude agglomerations for the most transit events within the first 2 hours. Instead we assume a nanoparticle density inside the cavity which allows 2 separate nanoparticles being simultaneously inside the larger TEM_{01} and TEM_{10} mode at the same time. In future measurements, a higher probability for measuring only a single nanoparticle with all three modes could be reached by reducing the concentration of the nanoparticle solution.

227 **Supplementary Figure 13: Data evaluation for the TEM₀₀, TEM₀₁ and**
 228 **TEM₁₀ mode**



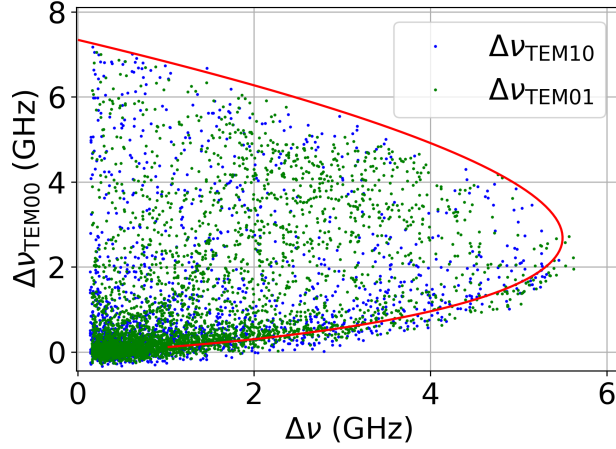
229 Here we show the measured raw data of the transit events, which is used for
 230 the calculation of the spatial coordinates of the SiO_2 nanoparticle with the size
 231 $r_{\text{hydr}} = 75.3 \text{ nm}$ (see Fig. 3b). In a), b) and c) the measured resonance linewidths
 232 of the TEM₀₀, the TEM₀₁ and the TEM₁₀ mode are depicted. d), e) and f) show
 233 the measured timeshifts, which are already recalculated in timeshift per linewidth
 234 units. g), h) and i) show the lineshift/linewidth with subtracted drift. More detailed
 235 information for the evaluation are given in Supplementary Fig. 5.

236 **Supplementary Figure 14: Noise measurement for the TEM₀₀, TEM₀₁**
 237 **and TEM₁₀ mode**



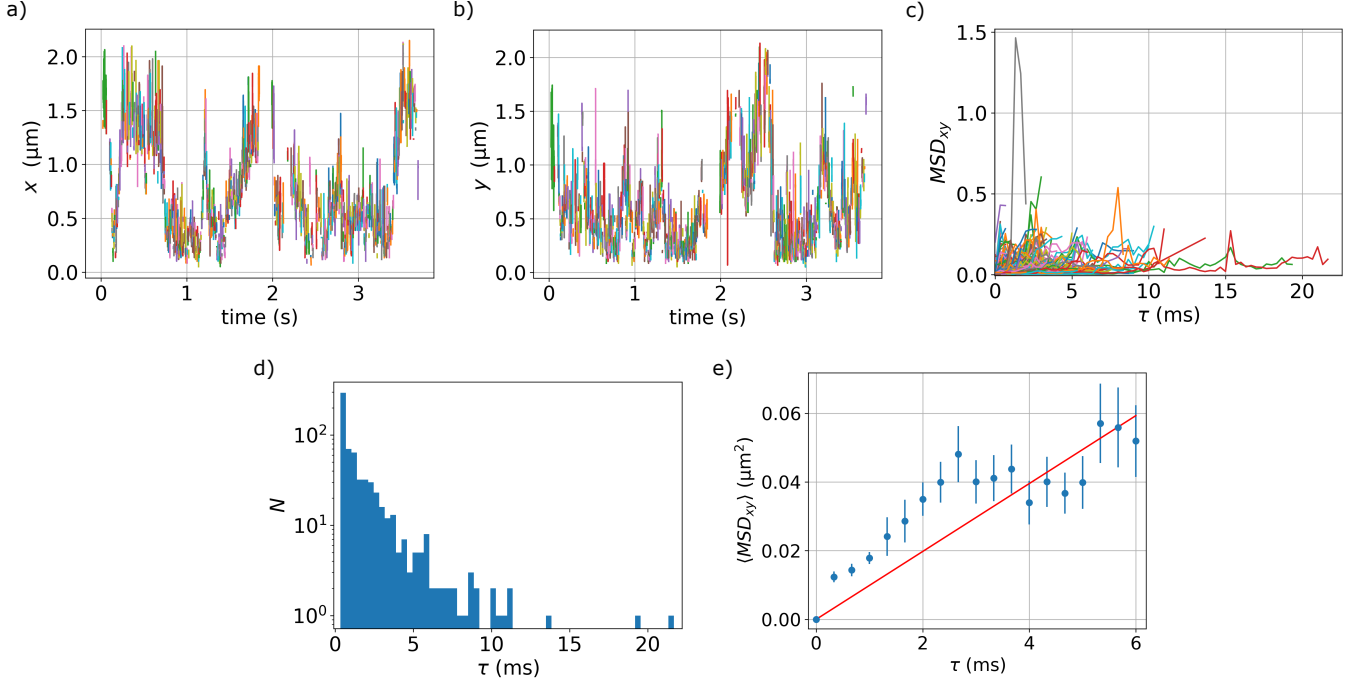
238 In order to deduce the noise form the measured frequency shifts in Fig. 3b, we
 239 plot the frequency shifts in an histogram. As already explained in Supplementary
 240 Fig. 5, the Gaussian fit to the measured counts at small frequency shift gives
 241 the measurement noise: $\sigma_{00} = 0.14$ GHz, $\sigma_{01} = 0.16$ GHz and $\sigma_{10} = 0.14$ GHz.

242 **Supplementary Figure 15: Correlated TEM₀₀ and higher order mode**
 243 **frequency shifts**



244 Here we show the correlation between the measured frequency shift of the funda-
 245 mental mode $\Delta\nu_{\text{TEM00}}$ and the higher order modes $\Delta\nu_{\text{TEM01}}$ ($\Delta\nu_{\text{TEM10}}$). When con-
 246 sidering particle locations for maximal coupling e.g. on the x -axis (i.e. $y = z = 0$),
 247 we can calculate the corresponding frequency shifts ($\Delta\nu_{\text{TEM00}}$, $\Delta\nu_{\text{TEM10}}$), see the red
 248 line in Fig. 14. This yields the maximally observable shift pairs ($\Delta\nu_{\text{TEM00}}$, $\Delta\nu_{\text{TEM10}}$)
 249 since particle displacements along x, z will reduce one or possibly both values. The
 250 density of position states leads to a larger probability to find small shift values and
 251 only very few datapoints close to the top part of the red contour line, in agreement
 252 with the data. The observed correlation confirms the validity of using the frequency
 253 shifts of the two modes for position determination.

254 **Supplementary Figure 16: Mean squared displacement**



255 From the spatial coordinates in Fig. 3d, the mean squared displacement (MSD) is
 256 deduced for the $x(t)$ - and $y(t)$ -propagation of the nanoparticle. Here we divide the
 257 movement in sequences: A new sequence i starts if one of the spatial coordinates
 258 x, y, z reaches a border of the sensing octant. There, the determined position is
 259 folded back into the octant, such that the absolute distance to earlier positions
 260 becomes meaningless, and therefore a new sequence starts. a) and b) show the
 261 division of $x(t)$ and $y(t)$ into different sequences by using different colors. For each
 262 sequence i , the two-dimensional MSD is calculated with the following definition [2]

$$MSD_i(\tau) = \frac{1}{T} \sum_{k=0}^T ((x_i(t + \tau) - x_i(t))^2 + (y_i(t + \tau) - y_i(t))^2)$$

263 and plotted in c) with different colors. The starting time for each sequence is set
 264 to zero. We derive the mean MSD $\langle MSD(\tau) \rangle$ by calculating the mean value from
 265 all sequences $MSD_i(\tau)$:

$$\langle MSD(\tau) \rangle = \frac{1}{N} \sum_i MSD_i(\tau)$$

266 Here, N is the number of MSD values at time τ and is plotted in d). One can see
 267 that the particles reach the sensing volume border within less than 10ms, which is

268 dominated by the diffusion along z where the available distance is only $\lambda/(4n_m)$. e)
 269 shows $\langle MSD(\tau) \rangle$ as a function of τ as well as the standard deviations σ_i as error
 270 bars. We observe a linear increase of $MSD(\tau)$, which is in agreement with free
 271 Brownian motion for the nanoparticle movement in x,y -directions. Hence, a linear
 272 fit to $\langle MSD(\tau) \rangle$ gives the diffusivity D of the nanoparticle:

$$D = \frac{1}{4} \frac{d}{d\tau} \langle MSD(\tau) \rangle.$$

273 Only for small τ , a good statistics is available (see number distribution in d)).
 274 Therefore, we only take the time window shown in e) for the fit (red). We also
 275 weighted the linear fit with the weighting function $w_i = 1/\sigma_i^2$. As a result,
 276 we get $D_{xy} = (2.47 \pm 0.67) \cdot 10^{-12} \text{ m}^2/\text{s}$. This gives a hydrodynamic radius of
 277 $r_{\text{hydr}} = k_B T / (6\pi\eta \langle D \rangle) = (86.9 \pm 23.6) \text{ nm}$.

278 **Supplementary Note 1: Cavity parameters for the different measure-**
 279 **ments**

280
 281 For our measurements we used two different kind of cavities: The cavity system
 282 shown in Fig. 1a (cavity 1) and the cavity shown in Supplementary Fig. 2 (cavity 2).
 283 In the following, the parameters of each cavity are specified and the results shown
 284 in the main article are related to the cavity systems used. In cavity 1, we measured
 285 SiO₂-spheres with hydrodynamic radius $r_{\text{hydr}} = 71.3 \text{ nm}$ (see Supplementary fig. 8)
 286 and in cavity 2 we measured SiO₂-spheres with hydrodynamic radius $r_{\text{hydr}} = 75.3 \text{ nm}$
 287 (see Supplementary Fig. 9).

	cavity 1	cavity 2
Finesse TEM ₀₀	18400	56710
Finesse TEM ₀₁	-	47789
Finesse TEM ₁₀	-	45668
Cavity length (μm)	27.3	5.4
FWHM TEM ₀₀ (MHz)	299	490
FWHM TEM ₀₁ (MHz)	-	581
FWHM TEM ₁₀ (MHz)	-	607
SM-Fiber: $r_{c,x}$ (μm)	62.4	46.1
SM-Fiber: $r_{c,y}$ (μm)	56.2	53.1
MM-Fiber: $r_{c,x}$ (μm)	58.9	79.2
MM-Fiber: $r_{c,y}$ (μm)	131.0	87.8
SM-Fiber transmission (ppm)	17.6	17.6
MM-Fiber transmission (ppm)	77	17.6
Fig. 2a		×
Fig. 2c	×	
Fig. 2d	×	
Fig. 2e		×
Fig. 3b		×
Fig. 3c		×
Fig. 3d		×
Fig. 3e		×
Fig. 3f		×

288
 289 FWHM is the linewidth of the respective cavity mode. The data shown in Fig. 1b
 290 and 3a were recorded by cavity 1 with slightly different cavity parameters (different

²⁹¹ cavity length, alignment) to those listed above.

Supplementary Note 2: Theoretical expected resonance amplitude decreases and frequency shifts

Depending on the nanoparticle position inside the cavity light field, different resonance amplitude decreases and frequency shifts occur. Both values reach their maximum value when the nanoparticle center is located at the antinode of the standing wave cavity light field. If the center is located at the node, a non-zero frequency shift occurs. This is due to the fact, that the nanoparticle hydrodynamical diameter is not negligible in comparison to the z -dimension of the antinode $\lambda/2n_m = 293\text{ nm}$. Therefore, we have to consider a weighted polarizability of the nanoparticle [3], which is calculated by integrating over the spherical nanoparticle volume:

$$\langle \alpha \rangle = \frac{\alpha}{V_p} \int_{V_p} dV_p \left(\frac{w_0}{w(z)} \right)^2 \exp^{\frac{-2(x^2+y^2)}{w(z)^2}} \cos^2(kz),$$

with the polarizability for a sphere

$$\alpha = 4\pi r^3 \epsilon_0 \frac{n_p^2 - n_m^2}{n_p^2 + 2n_m^2},$$

and using

$$w(z) = \frac{w_0}{\sqrt{1 + (z/z_0)^2}}$$

for the beam radius of the Gaussian light distribution and w_0 is the beam waist. The maximum frequency shift is then given by

$$\Delta\nu_{max} = \frac{\langle \alpha \rangle c}{2\lambda_m \epsilon_0 V_m}.$$

Here, λ_m is the laser wavelength in medium, c speed of light in vacuum, and $V_m = \pi w_0^2 d/4$ is the cavity mode volume.

For the simulation in Fig. 2b we assume a linear change in frequency shifts from 0 to $\Delta\nu_{max}$. The correlated resonance amplitude decreases can be calculated by the additional loss L_p originating from light scattering and absorption by the nanoparticle.

At first, we consider an empty cavity, though filled with water, but no nanoparticle

315 is disturbing the signal. The transmission through this cavity is determined by the
 316 losses L_1 , L_2 and the transmissions T_1 , T_2 of the two cavity mirrors and the water
 317 loss L_m :

$$T_0 = \frac{4T_1T_2}{(L_1 + L_2 + T_1 + T_2 + 2L_m)^2}.$$

318 When the nanoparticle enters the light field, it produces an additional loss L_p .
 319 Hence, the transmission can be expressed as

$$T(L_p) = \frac{4T_1T_2}{(2L_p + L_1 + L_2 + T_1 + T_2 + 2L_m)^2}.$$

320 The amount of loss L_p depends on the nanoparticle position inside the light field
 321 and reaches its maximum at the antinode, with

$$L_{p,\max} = \frac{4\sigma_{\text{ext}}}{\pi w_0^2}$$

and σ_{ext} being the extinction cross section of the nanoparticle and w_0 being the waist of the cavity light field. The extinction cross section depends on the size and refractive index of the nanoparticle and is taken from Mie Theory. For the nanoparticle losses L_p we assume a linear change between 0 and $L_{p,\max}$. The theoretical decrease of amplitude ΔT depending on the losses L_p produced by the nanoparticle can then be calculated as following:

$$\Delta T(L_p) = 100\% \left(1 - \frac{T(L_p)}{T_0} \right).$$

322 **Supplementary Note 3: Density of states - Theoretical frequency shift**
 323 **probability distribution for a single nanoparticle**

324
 325 Here we explain how we calculate the frequency shift probability distribution of
 326 the TEM₀₀ mode, which we use to fit the data and thereby deduce the refractive
 327 index (see Supplementary Fig. 8).

328
 329 Depending on the position (x_0, y_0, z_0) of the nanoparticle inside the TEM₀₀ mode,
 330 an according frequency shift $\Delta\nu(x_0, y_0, z_0)$ occurs:

$$\Delta\nu(x_0, y_0, z_0) = \frac{\langle\alpha\rangle_{00}c}{2\lambda_m\epsilon_0V_m}, \quad (1)$$

331 with the weighted polarizability

$$\langle\alpha(x_0, y_0, z_0)\rangle_{00} = \frac{\alpha(n_p)}{V_p} \int_{V_p} dV_p \cdot I_{\text{Gauss}} \cos^2(k(z - z_0))$$

332 and the Gaussian intensity distribution

$$I_{\text{Gauss}} = \left(\frac{w_0}{w(z - z_0)} \right)^2 \exp \frac{-2((x-x_0)^2+(y-y_0)^2)}{w(z-z_0)^2}.$$

333 Here, $k = 2\pi n_{\text{H}_2\text{O}}/\lambda_{780}$ is the wavenumber depending on the wavelength in water
 334 $\lambda_{780}/n_{\text{H}_2\text{O}}$. For a given refractive index n_p , the theoretical frequency shift proba-
 335 bility distribution can be calculated and subsequently the derived frequency shift
 336 values plotted in an histogram.

337

338 **Supplementary Note 4: Theoretical frequency shift matrices for the**
 339 **calculation of the 3D track**

340
 341 In Supplementary Note 3 we already introduced the calculation of the theoretical
 342 frequency shift matrix of the fundamental mode. Equation (1) (Supplementary Note
 343 3) can be also used for the calculation of the TEM₀₁ and TEM₁₀ matrices, but the
 344 polarizabilities have to be adapted to

$$\langle \alpha(x_0, y_0, z_0) \rangle_{01} = \frac{\alpha(n_p)}{V_p} \int_{V_p} dV_p \cdot \frac{8(x - x_0)^2}{w_{01}(z - z_0)^2} I_{\text{Gauss}} \cos^2(k_{01}(z - z_0))$$

for the TEM₀₁ mode and

$$\langle \alpha(x_0, y_0, z_0) \rangle_{10} = \frac{\alpha(n_p)}{V_p} \int_{V_p} dV_p \cdot \frac{8(y - y_0)^2}{w_{10}(z - z_0)^2} I_{\text{Gauss}} \cos^2(k_{10}(z - z_0))$$

345 for the TEM₁₀ mode. In addition, we have to change the wavenumber to
 346 $k_{01} = k_{10} = 2\pi n_{\text{H}_2\text{O}}/\lambda_{785}$, since we probe the higher modes at a different wave-
 347 length (see Supplementary Fig. 1).

348
 349 In order to deduce the spatial coordinates of the nanoparticle from the measured
 350 frequency shifts, the latter are compared with the theoretical frequency shift values.
 351 For the theoretical shift matrices we choose spatial pixel steps with 16.9 nm in lateral
 352 directions (x, y) and 1.6 nm in longitudinal direction (z). A suitable pixel size can
 353 be estimated from the measured frequency noise of each mode (see Supplementary
 354 Fig. 13). By including the measurement noise to the measured frequency shifts, we
 355 find multiple possible positions of the nanoparticle inside the theoretical frequency
 356 shift matrices at measurement time t_k . As a tracking algorithm we take from the
 multiple possible position the one which is closest to the earlier position at time t_{k-1} .

357

358

BIBLIOGRAPHY

- 360 [1] Y. T.C. Ko, J. P. Huang, and K. W. Yu. The dielectric behaviour of single-shell spherical cells with a dielectric anisotropy
361 in the shell. *Journal of Physics Condensed Matter*, 16(3):499–509, 2004.
- 362 [2] Vincent Tejedor, Olivier Bénichou, Raphael Voituriez, Ralf Jungmann, Friedrich Simmel, Christine Selhuber-Unkel, Lene B.
363 Oddershede, and Ralf Metzler. Quantitative analysis of single particle trajectories: Mean maximal excursion method.
364 *Biophysical Journal*, 98(7):1364–1372, 2010.
- 365 [3] A. A.P. Trichet, P. R. Dolan, D. James, G. M. Hughes, C. Vallance, and J. M. Smith. Nanoparticle Trapping and Charac-
366 terization Using Open Microcavities. *Nano Letters*, 16(10):6172–6177, 2016.